High-Thrust 2-D CoFlow Jet Cylinder Wind Sail at Varying Angles of Attack

Zhijin Lei, *Yan Ren, †Brendan McBreen ‡and Gecheng Zha §
Dept. of Mechanical and Aerospace Engineering
University of Miami, Coral Gables, Florida 33124
E-mail: gzha@miami.edu

Abstract

This paper numerically studies the performance of a 2D CoFlow Jet cylinder wind sail at different angle of attack and jet strength. The cylinder sail is simulated using the in-house Reynolds-averaged Navier-Stokes (RANS) solver, FASIP, with Spalart-Allmaras (SA) turbulence model. A 3rd order WENO scheme is used to resolve the Navier-Stokes equations. The dual-time step method is used for unsteady simulation. A comparative analysis of the lift coefficients, drag coefficients and energy expenditure at various jet momentum coefficients and angles of attack are conducted. When $C_\mu = 0.5$, the lift coefficient at zero angle of attack reaches 12.63. The power coefficient at this flow condition is only 5% of C_L, resulting in a $C_L/C_{D,c}$ of 19.92. When C_μ is increased to 2.0, the lift coefficient reaches 25.13, about doubled, but the power coefficient is increased exponentially by 10 times. As AoA varies from -90° to 90°, the lift does not vary much within AoA of ±20° at high C_L level of 20. At a lower C_L level of 12, the C_L has a much broader insensitive range to AoA from -20° to +60°. The drag coefficient and CFJ power coefficients are also similar. The numerical results of 2D CFJ cylinders indicate that the CFJ cylinder has the potential to provide very high lift coefficient at low drag and low power consumption with a large tolerance range of AoA. Such features are very beneficial as rigid wind sails for shipping.

Nomenclature

AoA	Angle of Attack
AFC	Active Flow Control
AR	Aspect Ratio
CFJ	Co-Flow Jet
C_D	Drag coefficient
C_L	Lift coefficient or Propulsion Coefficient
$C_{L,max}$	Maximum lift coefficient
C_M	Moment coefficient
C_P	Pressure coefficient, positive unless declared
$C_{p,sh}$	Constant pressure specific heat
C_{Thrust}	Thrust coefficient, $C_L \cdot \cos AoA + C_D \cdot \sin AoA$;
C_μ	Jet momentum coefficient, $\dot{m}_j U_j/(q_\infty S)$

---

* Graduate Student.
† Research Engineer.
‡ Graduate Student.
§ Professor, ASME Fellow, AIAA associate Fellow.

D	Total drag on the sail
D_{cyl}	Diameter of the sail cylinder
FASIP	Flow-Acoustics-Structure Interaction Package
H_t	Total enthalpy
L	Total lift on the sail
$\dot{m}$	Mass flow
M	Mach number
M_{is}	Isentropic Mach number
P	CFJ pumping power, $\dot{m}C_p T_{t,2}\ (\Gamma^{(\gamma-1/\gamma)}-1)/\eta$
P_c	Power coefficient of CFJ, $P/0.5\rho_\infty U_\infty^3 S$
PR	Total pressure ratio, Γ
P_t	Total pressure
RANS	Reynolds-Averaged Navier-Stokes
Re	Reynolds number
S	Planform area of the sail
T_t	Total temperature
U_∞	Freestream velocity
ZNMF	Zero-Net Mass Flux
$(C_L/C_D)_c$	Aerodynamic efficiency corrected for CFJ, $C_L/(C_D + P_c)$
C_L^2/C_D	Productivity efficiency coefficient
$(C_L^2/C_D)c$	Productivity efficiency coefficient corrected for CFJ, $C_L^2/(C_D + P_c)$
c	Subscript, stands for corrected
j	Subscript, stands for jet
γ	Air specific heats ratio
η	CFJ pumping system efficiency
∞	Freestream

1   Background

Global marine shipping delivers over 80% of the goods in the world[1]. As the Paris Agreement comes into effect, there is an increasing demand to reduce marine shipping fossil fuel consumption and carbon emissions. A part of this demand can be realized by introducing rigid wind sails to modern ships[2], which use the wind energy to generate a part of the propulsion force.

Various types of sails are described by Marchay[3]. The early sails' usage can be dated back to the sixth century BC according to archaeological studies on Cucuteni-Trypillian culture ceramics[4]. Flettner rotor spinning is an effective flow control technique to generate high lift coefficient by spinning the cylinder in the same direction of the incoming flow, as shown in Fig. 1.
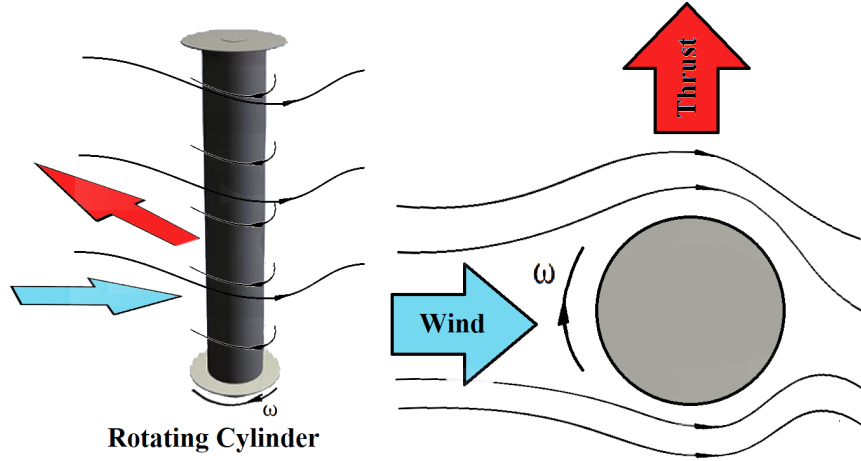
Figure 1: A Flettner Rotor under the Magnus Effect.

Figure 2: Current Sail Types and Their Average Aerodynamic Performances, from[5].

In the first few decades after the appearance of the Flettner rotor, the lift(propulsive) force generated by the device is too low to propel ships due to the low cylinder spinning speed, and thus the applications are rare. Some large scale Flettner rotors have been used in cargo ships since 2000s. Fig. 2 shows a comparison of the recent major sail types. The Flettner rotor sail generates the highest maximum lift coefficient among the existing rigid wind sail techniques. However, Flettner rotor requires spinning the whole cylinder. When the cylinders are large in size for ship usage, spinning them requires complex system and also leads to high energy consumption.

1.1 Concept of CoFlow Jet Cylinder Wind Sail

CoFlow Jet flow control is a zero-net-mass-flux control technique originally developed by Zha and his team for aircraft airfoil [6, 7, 8, 9, 10, 11, 12, 13, 14, 15, 16, 17]. It demonstrates ultra-high lift coefficient, wide stall margin,

2

and low energy expenditure.

Yang and Zha [18] first apply CFJ to cylinders and achieve a lift coefficient as high as C_L=28. However, their work is more focused on the aerodynamic performance, does not consider much on the energy efficiency. McBreen *etal* [19] enlarge the injection and suction slot sizes that reduce the CFJ power required dramatically. Their work indicates that CFJ cylinders can be used as rigid wind sails for shipping like the Flettner rotors, but do not need to spin the cylinders.

Fig. 3 shows a conceptual ship equipped with CFJ-sail matrix, where the center of gravity is assumed to be between front and back sails, and thus the momentums from different sails cancel out with each other.
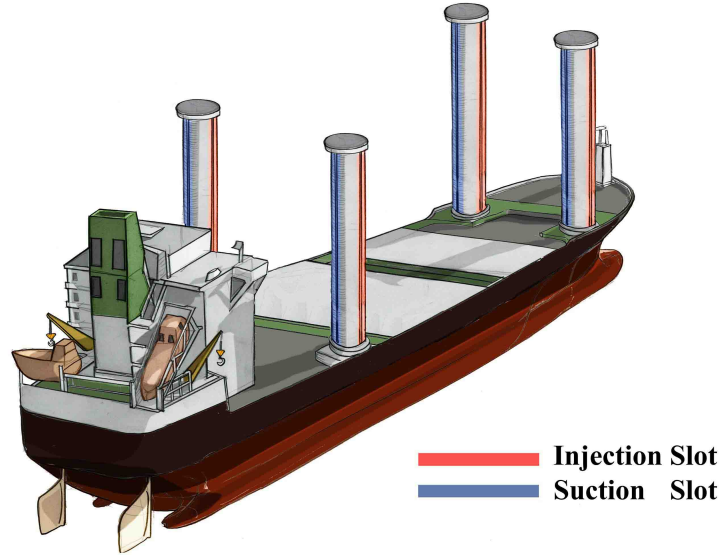
Figure 3: A Conceptual CFJ-Sail Ship.
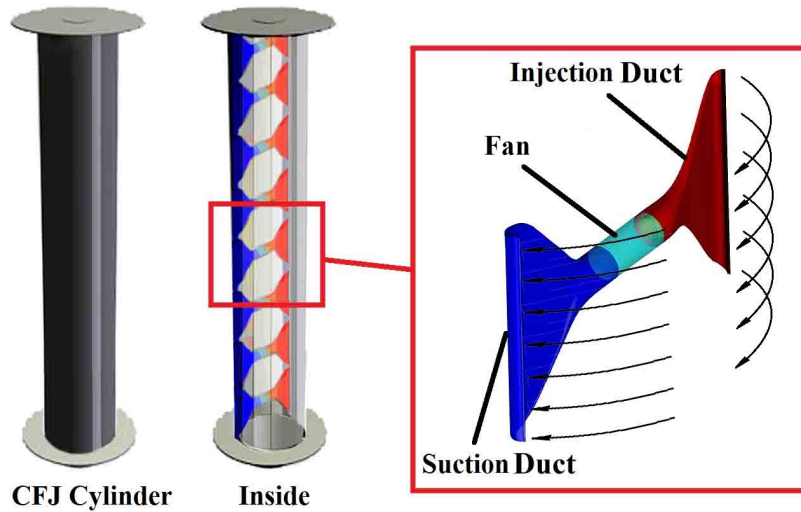
Figure 4: A Sketch of the CFJ Sets Inside the CFJ-Sail.

As shown in Fig. 4, for a segment of CFJ cylinder, the injection slot and the suction slot are connected by

a pair of well-designed ducts with a fan in the middle. A small amount of mass flow is drawn into the suction duct, pressurized and energized, and then injected tangent to the cylinder wall surface via an injection duct. As mentioned above, the whole process does not add any mass flow to the system, and hence forms a zero-net-mass-flux(ZNMF) flow control. The purpose of this paper is to study the CFJ cylinder wind sails performance at different angle of attack and injection jet momentum coefficient.

2 Parameters

This section lists important parameters to evaluate aerodynamic performance of a Flettner rotor and a CFJ cycle.

2.1 Jet Momentum Coefficient

The jet momentum coefficient C_μ is a parameter used to quantify the jet intensity. It is defined as:

$$C_\mu = \frac{\dot{m}U_j}{\frac{1}{2}\rho_\infty U_\infty{}^2 S} \tag{1}$$

where $\dot{m}$ is the injection mass flow, V_j is the mass-averaged injection velocity, ρ_∞ and V_∞ denote the free stream density and velocity, and S is the planform area of the sail.

2.2 Power Coefficient

For CFJ, which is implemented by mounting a fan pumping system inside the cylinder, the power consumption is determined by the jet mass flow and total enthalpy change as the following:

$$P = \dot{m}(H_{t1} - H_{t2}) \tag{2}$$

where H_{t1} and H_{t2} are the mass-averaged total enthalpy in the injection cavity and suction cavity respectively, P is the Power required by the pump and $\dot{m}$ the jet mass flow rate.

Introducing P_{t1} and P_{t2} the mass-averaged total pressure in the injection and suction cavity respectively, the pump efficiency η, and the total pressure ratio of the pump $\Gamma = \frac{P_{t1}}{P_{t2}}$, the power consumption is expressed as:

$$P = \frac{\dot{m}C_{p,sh}T_{t2}}{\eta}(\Gamma^{\frac{\gamma-1}{\gamma}} - 1) \tag{3}$$

where γ is the specific heat ratio equal to 1.4 for air, the power coefficient P_c is expressed as:

$$P_{c,CFJ} = \frac{P}{\frac{1}{2}\rho_\infty V_\infty^3 S} \tag{4}$$

4

3 CFD Simulation

3.1 CFD Code

The in-house high-accuracy CFD code Flow-Acoustics-Structure Interaction Package (FASIP) is used to conduct the numerical simulation. The 3D Reynolds averaged Navier-Stokes (RANS) equations with one-equation Spalart-Allmaras(SA) turbulence model is used. A 3rd order WENO scheme for the inviscid flux and a 2nd order central differencing for the viscous terms are employed to discretize the Navier-Stokes equations. The low diffusion E-CUSP scheme used as the approximate Riemann solver suggested by Zha *et al* [20] is utilized with the WENO scheme to evaluate the inviscid fluxes. Implicit time marching method using Gauss-Seidel line relaxation is used to achieve a fast convergence rate [21]. Parallel computing is implemented to save wall clock simulation time. The RANS solver is validated for CFJ airfoil simulations [22].

3.2 Models and Meshes

The cylinder sail used in the two-dimensional simulation is depicted in Fig. 5. The diameter of the cylinder is one meter(based on which the Reynolds number is calculated), and the farfield boundary (radius) of the computational domain is 168 times of the cylinder diameter. As shown in Fig. 5(a), the suction surface (upper surface) of the CFJ cylinder is slightly translated downward to accommodate the tangential injection jet. This distance is named suction surface translation (SST). In this model, the SST is 0.01 meter or 1% of the cylinder diameter, which is identical to the injection slot size. At the angle of attack (AoA) of zero degree, a line connecting injection slot and cylinder's rotation center (center of circle) is perpendicular to the X-axis, and the suction duct is located 112.5 degrees clockwise(downstreamward) from that location. The suction slot size is 0.025 meter or 2.5% of the cylinder diameter.
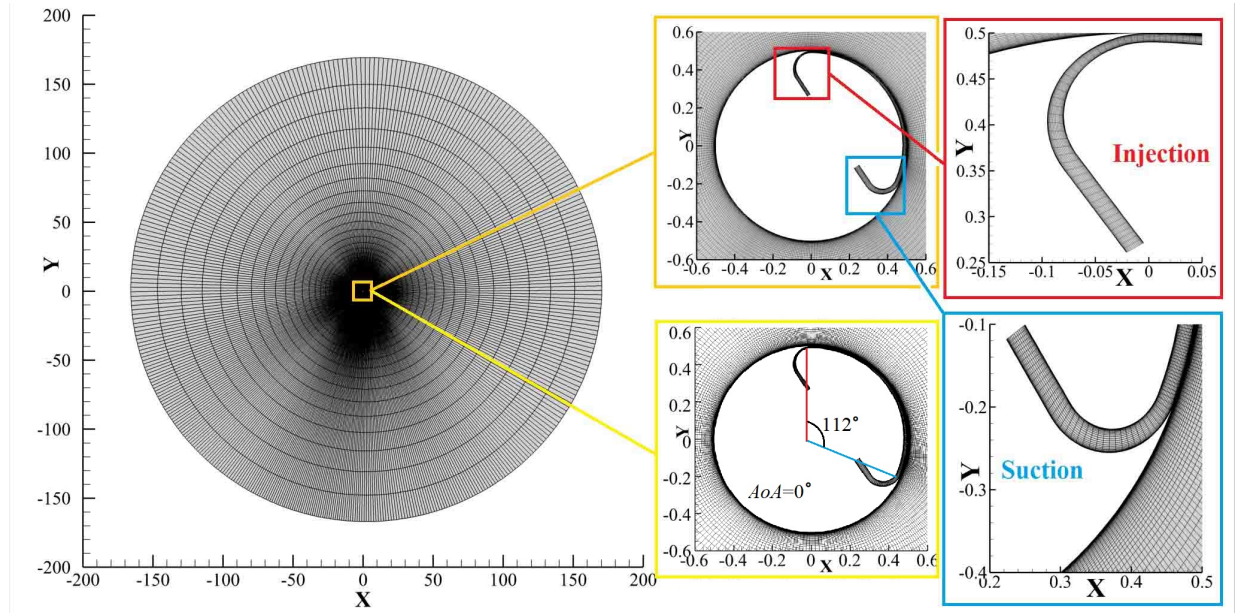

Figure 5: 2-D Mesh Computational Domain and Near-Wall Mesh of CFJ-Cylinder.

The mesh is constructed using the O-mesh topology in order to achieve high quality around the airfoil. The

farfield mesh around cylinder has a size of 38,200 cells with 320 points around the cylinder and 120 points in the radial direction, while the CFJ part has 7,200 cells of 40×180 in the streamwise direction and transverse direction for CFJ ducts. The O-meshes are split into multiple blocks for the parallel computing. To resolve the turbulent boundary layer, the thickness of the first layer around the surface has $y_+ = 1$.

Table 1: Comparison of aerodynamic performances of a 2-D CFJ cylinder versus mesh density, $AoA=0°$.

Mesh Size	C_L	C_D	C_M	P_c
45,400(Baseline)	12.63	0.061	0.131	0.573
55,600	12.61	0.060	0.134	0.579
130,560	12.60	0.061	0.131	0.573

A mesh independence analysis is conducted with three refined mesh sizes of 45,400 ($120 \times 320 + 180 \times 40$), 55,600 ($121 \times 400 + 180 \times 40$) and 130,560 ($120 \times 968 + 180 \times 80$) respectively. Table 1 indicates that the numerical solutions are converged with the mesh size and the results discrepancy is within 1%. Thus the mesh size of 45,400 is sufficient to achieve mesh independent solutions.

3.3 CFJ Boundary Conditions

The wall treatment suggested in [23] to achieve the 3rd order accuracy is employed. Total pressure, total temperature and flow angle are specified as the inlet boundary conditions for the upstream side of the far-field boundary and inside the injection cavity. Constant static pressure is used downstream at the far-field boundary and in the suction cavity.

To achieve zero-net mass-flux with the CFJ flow control, the injection mass flow must be equal to the mass flow entering the suction slot. Additionally, the jet strength must be controlled in order to reach the prescribed C_μ. This is achieved by iterating the jet total pressure until the C_μ value is within 1% of the prescribed value. At the suction, the suction mass flow is matched to the injection mass flow by iterating the static pressure at the suction cavity. The process is iterated throughout the simulation until the specified momentum coefficient is achieved and the injection and suction mass flow match.

4 Results and Discussion

The free-stream condition of $Ma=0.05$ and $Re = 1.36$ millions are used in this study. As mentioned earlier, the reference length is defined as the diameter of the supposed real cylinder of 1 meter, the static pressure is 1 atm, the freestream density is 1.225 kg/m^3 and the static temperature is 288.15K. The physical time step in unsteady simulations is 0.025.

4.1 Cylinder Cylinder Performance and CFJ with Jet Momentum Coefficients

The flowfields around CFJ cylinders with $C_\mu=0.5$, $C_\mu=1.0$ and $C_\mu=2.0$ are shown in Fig. 6. The angle of attack is defined to be 0° when the injection slot position is at the 12 o'clock position with the incoming flow in the horizontal direction from the left. The high-speed region around the upper surface of cylinder becomes larger as jet momentum coefficient increases, which increases the pressure difference between upper surface("suction

6

surface") and lower surface("pressure surface") of cylinder. Fig. 7a shows the cylinder surface pressure coefficient and Isentropic Mach number distributions. It can be seen that, as C_μ increases, the area enclosed by the C_p and isentropic Mach number is also enlarged, indicating an increase of the lift coefficient.

(a) C_μ=0.5   (b) C_μ=1.0   (c) C_μ=2.0
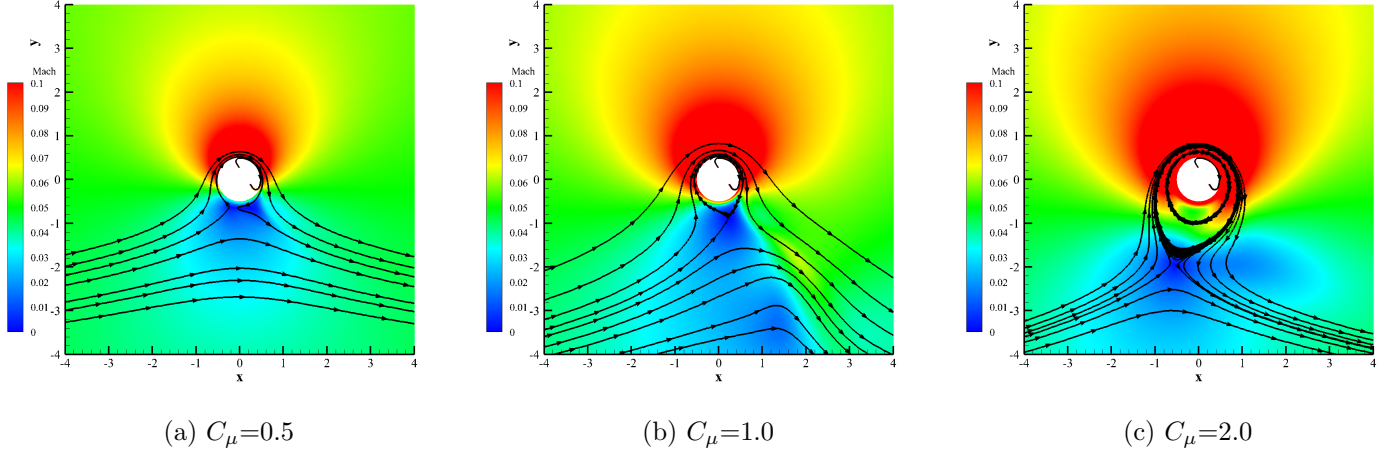
Figure 6: Mach Number Contoured Flowfields of Varied C_μs of CFJ Cylinders at AoA=0°.

(a) Negative C_P.   (b) Isentropic Mach Number.
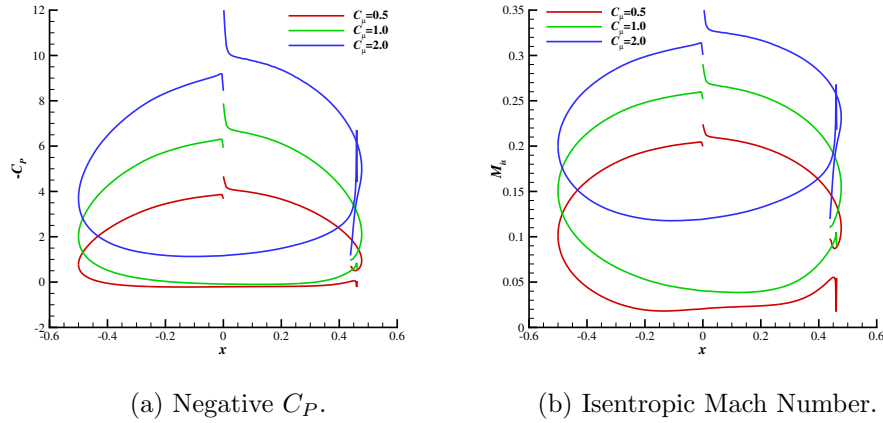
Figure 7: Negative C_P and M_{is} Distribution Along the CFJ and Rotating Cylinders at AoA=0°.

The C_L, C_D, C_M, P_c, C_L/C_D and $C_L/C_{D,c}$ between CFJ sails with varied C_μs at AOA=0° are compared in Table 2. It can be seen that, by introducing a CFJ of C_μ=0.5 to the cylinder, a lift coefficient of 12.63 is reached at $AoA = 0°$. The power coefficient at this flow condition is only 4.5% of C_L, resulting in a C_L/P_C of 22.04. When C_μ is further increased to 2.0, the lift coefficient is doubled, but the power coefficient is increased by tenfold, indicating the cost to increase lift coefficient grows exponentially. However, since the net thrust power is the subtraction relationship between the thrust and the power coefficient, the high lift and high power mode will generate substantial propulsive power when the wind is from the side at low AoA.

Table 2 indicates that the CFJ power coefficient increases exponentially with the lift coefficient. From the C_L of 12.63 to 25.13, the lift is about doubled, but the CFJ power coefficient is increased 10 fold. The drag coefficient is also largely increased at C_L of 25.13. It is mostly because the stagnation region is shifted to the upstream side of the cylinder that contributes a large pressure drag component.

7

Table 2: Comparison of C_L, C_L/C_D and other performances between CFJ sails, $AOA=0°$.

CFJ. C_μ	C_L	C_D	C_M	P_c	C_L/C_D	C_L/P_C
0.5	12.63	0.061	0.131	0.573	207.05	22.04
1.0	20.12	0.142	0.192	1.81	141.69	11.12
2.0	25.13	1.591	-0.115	6.25	15.80	4.02

4.2 Angle of Attack Effect

A schematic of angle of attack(AOA), thrust and lift coefficient are shown in Fig. 8. The AoA is defined as the angle between the thrust vector, which is determined by the location of injection slot, and the lift vector, which is perpendicular to the freestream direction. Thus, a thrust coefficient can be described by coefficients of lift and drag:

$$C_{Thrust} = C_L \cdot cosAoA + C_D \cdot sinAoA \tag{5}$$
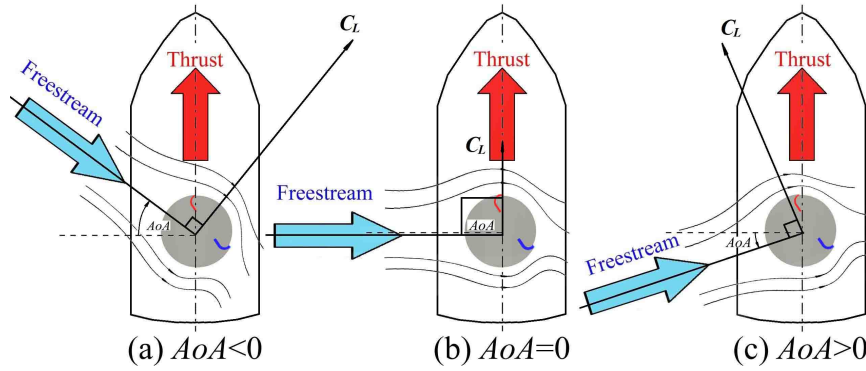
Figure 8: A Schematic of AoA, Thrust and Lift Definitions.

By taking the time average of the periodically oscillating results, the lift, drag and power coefficient of CFJ cylinders versus angles of attack are plotted in Fig. 9 for the case of C_μ of 0.5 and 1.0. For the $C_\mu = 0.5$ cases, the range of AoA is investigated from -90° to 90°, while for the $C_\mu = 1.0$ cases, the range of AoA is investigated from -50° to 50°.

It can be seen from Fig. 9(a) that, due to the coflow jet effect on the cylinder leeward (downstream) region, both the lift curves at C_μ 0.5 and 1.0 show similar trends:

As the AoA decreases from -90° (headwind), the lift coefficient C_L increase almost linearly and reaches the maximum at -25° and -20° respectively with a C_L of 13.53 and 20.8. After the C_L peak, the C_L is fairly stable and decreases slightly until it stalls at AoA of 20° for the C_μ 1.0 case and at AoA of 70° for the C_μ 0.5 case. After the stall AoA, the lift drops sharply. Even though the lift coefficient drops a lot after the stall for the C_μ 1.0 case, the lift coefficient remains a a very high value of 12. A combined thrust force coefficient from Eq. 5 versus AoA is depicted in Fig. 9(c), which shows a very smooth magnitude transit for the C_μ 0.5 case while the trace of stall at $C_\mu = 1.0$ is still observed.

8

(a) Lift Coefficient.

(b) Drag Coefficient.

(c) Thrust Coefficient.

(d) Power Coefficient.

(e) Sketch of C_{Thrust} magnitude.

Figure 9: Time-Averaged Lift, Drag, Power Coefficient and Thrust Versus Angle of Attack.

Fig. 9(b) shows the variation of drag coefficients as AoA rises. Compared with lift coefficients, drag coefficient values are generally two orders of magnitude lower except in the stall region with $C_\mu = 0.5$, where drag coefficient dramatically climbs to the same order of magnitude of the local C_L. It is also noticed that, the drag coefficient does not vary much with the jet momentum efficient. However, the power coefficient results in Fig. 9(d) indicates that P_c highly depends on both C_μ and AoA. When the jet flow intensity is low, power consumption remains around 0.6 with a wide range of AoA from -80° to 40°, and then rise largely. When C_μ is increased from 0.5 to 1.0, the power coefficient increases by 417.8%, 316.2% and 366.2% at AoA = -50°, 0° and 50° respectively, while the drag coefficients almost remain identical considering the scale. For the 2-D situation, the power coefficient is a more dominant factor reducing the net thrust power. Fig. 9(e) sketches one of the CFJ sail's important advantages over the Flettner rotor: By controlling the heading of injection slots, it can provide considerable net thrust in a wide range of relative bearing at a given wind direction, without the need of rudder balance.
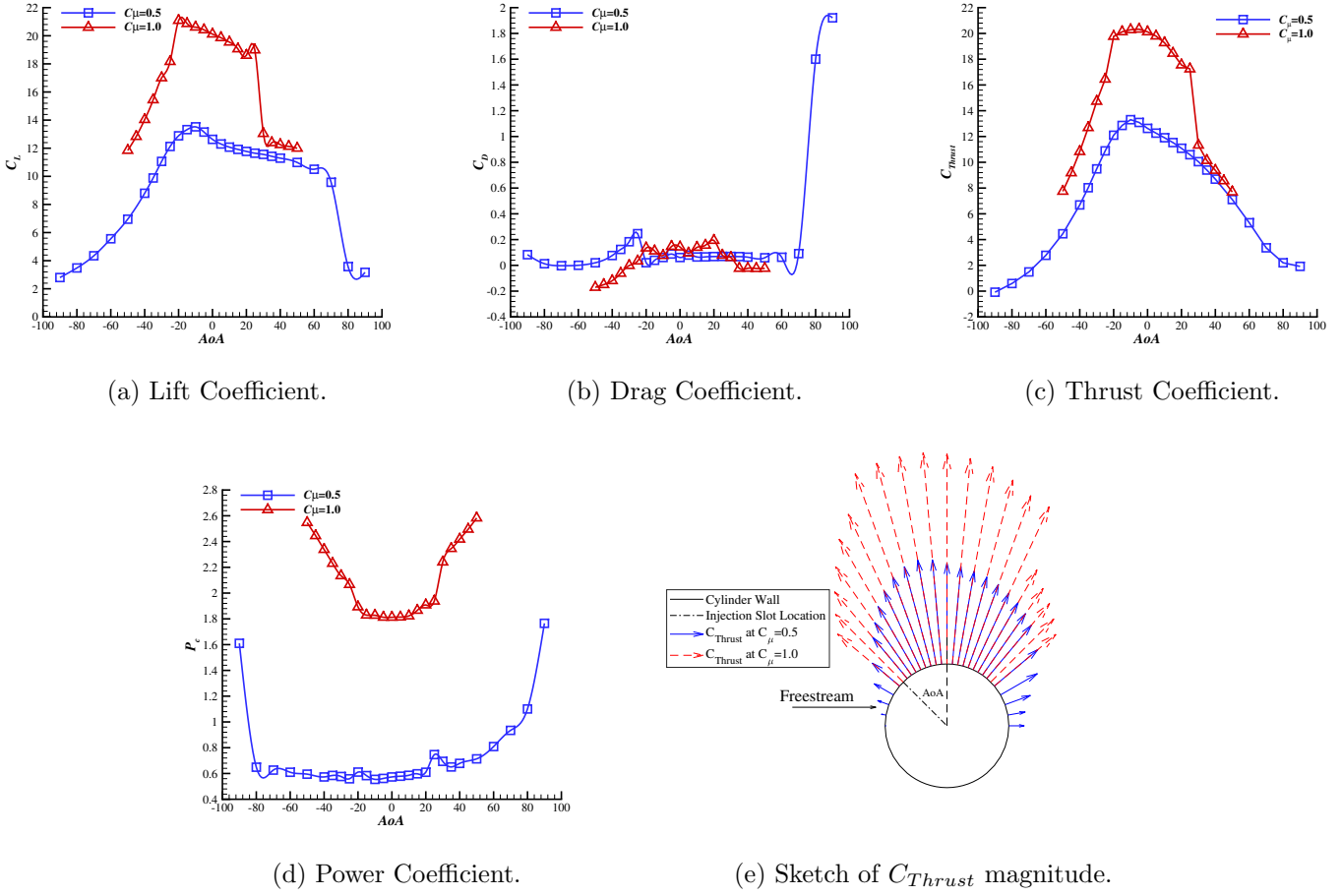
By taking the time average of the periodically oscillating results, the lift-drag ratio, C_L/P_c and corrected aerodynamic efficiency of CFJ cylinders versus angles of attack are plotted in Fig. 10. Due to the large lift enhancement and very small or even negative drag, the C_L/C_Ds are extremely large, and some abnormal values caused by near-zero C_D are ignored. Note that the negative C_L/C_D is due to the negative drag coefficient, meaning it is very good, better than the value of infinity generated by a zero drag. A more meaningful index is $C_L/C_{D,c}$ shown in Fig. 10(c), which has a similar shape to C_L/P_c in Fig. 10(b). The $C_L/C_{D,c}$ reaches its maximum at

AoA = -10° with both of the C_μ values. When C_μ = 0.5, the maximum $C_L/C_{D,c}$ value is 22.01, while when C_μ = 1.0, the maximum value is 10.83, decreased by 50.8%.

(a) C_L/C_D.

(b) C_L/P_c.

(c) Corrected Aerodynamic Efficiency.
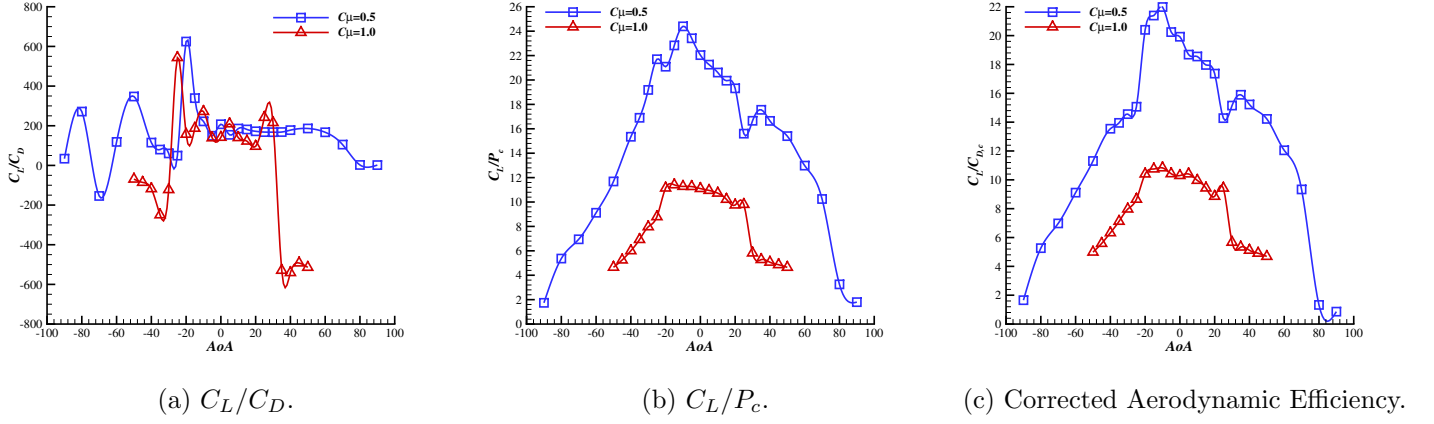
Figure 10: Time-Averaged Lift-Drag Ratio, C_L/P_c and Corrected Aerodynamic Efficiency Versus Angle of Attack.

(a) AOA=-80°(Average).

(b) AOA=-60°.

(c) AOA=-40°.

(d) AOA=-20°.

(e) AOA=20°.

(f) AOA=40°.

(g) AOA=70°.

(h) AOA=80°(Average).
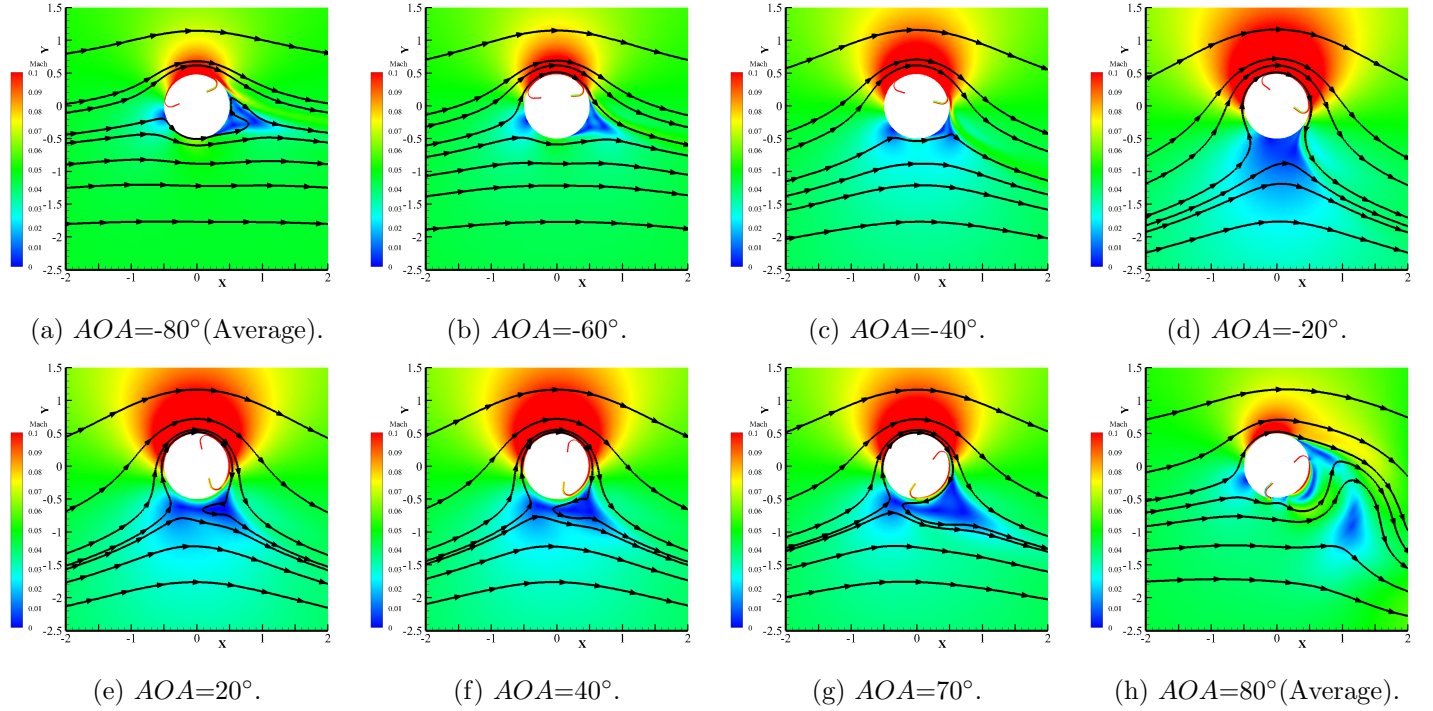
Figure 11: Mach contours of flowfields around the CFJ cylinders with C_μ of 0.5 as AoA increases from -80° to 80°.

Fig. 11 illustrates the Mach contours of flowfields around the CFJ cylinders with C_μ of 0.5 as AoA increases from -80° to 80°. Note that the flow always comes from left side horizontally. The AoA variation is made by rotating the cylinder. As previously defined, the AoA=0° is the position that the injection slot is at 12 o'clock position. It can be seen that, the CFJ can attach the flow for the majority range of the AoA except near the two stall AoAs.

10

4.3 Unsteadiness due to Angles of Attack and Jet Momentum Coefficient

When the CFJ C_μ is as large as 1.0 or 2.0, or when the AoA is large enough to make the cylinder stall, the flow around the cylinder becomes unstable with oscillatory C_L, C_D and other aerodynamic parameters.

To investigate the characteristics of the phenomenon, the lift coefficients with C_μ of 0.5 and 1.0 versus characteristic time are plotted in Fig. 12(a) and (b) respectively. Fig. 12(a) indicates that, with $C_\mu = 0.5$, CFJ can generate stable lift coefficient at most of the AoAs. Only AoAs of 80° and 90° leads to significant C_L performance oscillation. The oscillation periods and magnitudes of $AoA = 80°$ are shown in Fig. 12(a), where the oscillation magnitude is 39.7% of $C_{L,average}$, and the oscillation period is 5.94 characteristic times with a reduced frequency of 0.168. As AoA further increases, the cylinder is deeper stalled, resulting in a larger magnitude and period. For the $AoA = 90°$ case, the magnitude is 59.2% of $C_{L,average}$, and the period is 7.23 characteristic times with a reduced frequency of 0.138.

When the C_μ is increased to 1.0, the oscillatory results are mostly at the high lift regime at low AoA (sidewind). When $AoA = 0°$, the oscillation magnitude is 5.2% of $C_{L,average}$, and the oscillation period is 23.18 characteristic times. When $AoA = -20°$, the oscillation magnitude is only 3.6% of $C_{L,average}$, and the period is 11.12 characteristic times. When AoA moves to 20°, the oscillation magnitude becomes 9.5% of $C_{L,average}$, and the period is also increased to 23.17 characteristic times.

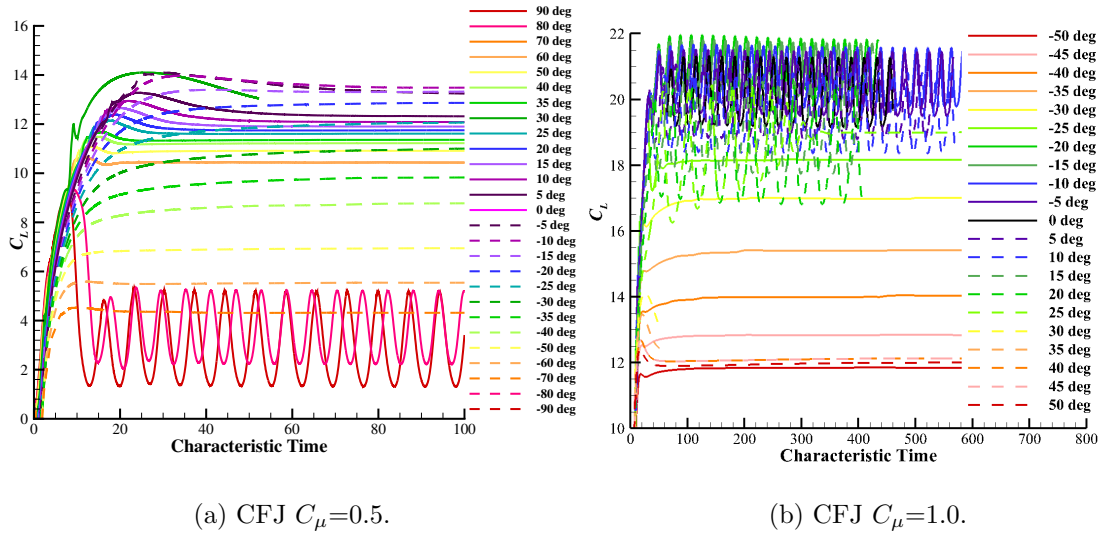(a) CFJ C_μ=0.5. (b) CFJ C_μ=1.0.

Figure 12: Numerically Simulated Lift Coefficient versus the Characteristic Time.

Fig. 13 and Fig. 14 shows the drag and power coefficients at different AoAs with $C_\mu = 0.5$ and 1.0 versus characteristic time respectively, where similar effects are observed.

11

(a) CFJ C_μ=0.5.

(b) CFJ C_μ=1.0.
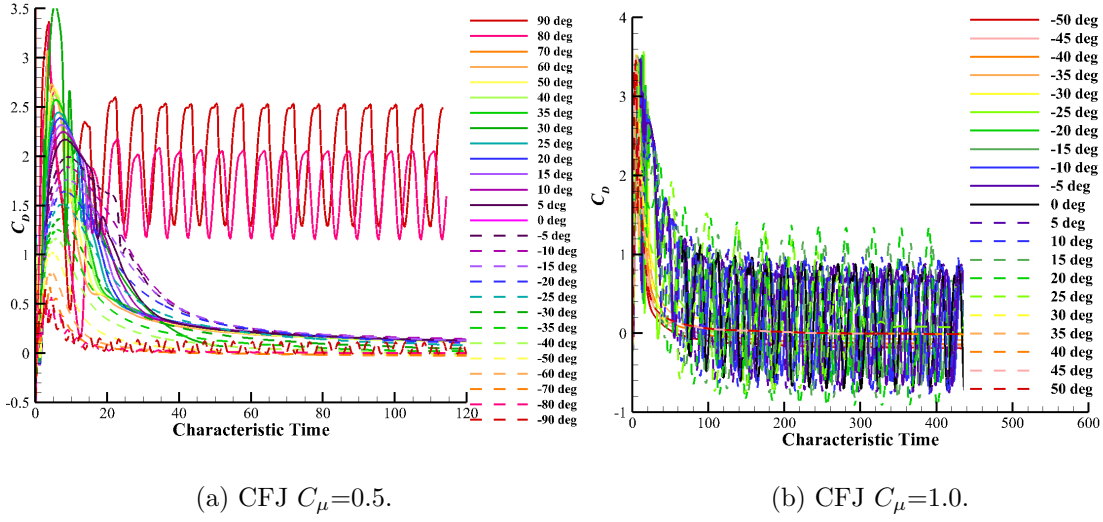
Figure 13: Numerically Simulated Drag Coefficient versus the Characteristic Time.

(a) CFJ C_μ=0.5.

(b) CFJ C_μ=1.0.

Figure 14: Numerically Simulated Power Coefficient versus the Iteration Time.

There are two oscillation modes observed. The first oscillation mode is attributed to stall, for which the flow is separated due to the low C_μ that cannot maintain the flow attached. This mode will in general have low lift coefficient due to flow separation, as shown in Fig. 15.

12

(a) t/P=0.25. (b) t/P=0.5. (c) t/P=0.75. (d) t/P=1.0.

Figure 15: Mach Contours of Flowfields around the CFJ Cylinder with C_μ of 0.5, AoA=80° in a Period.
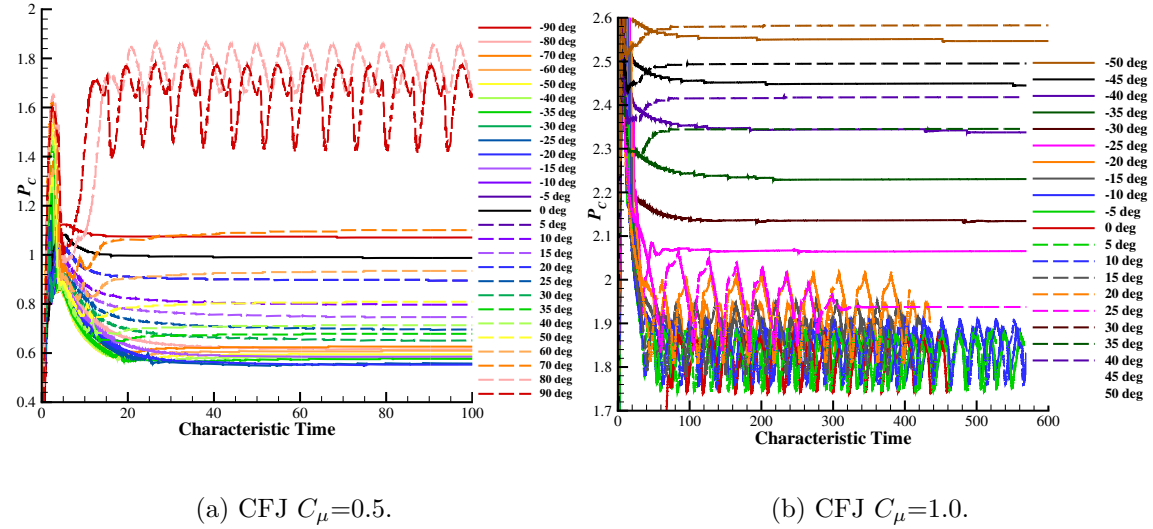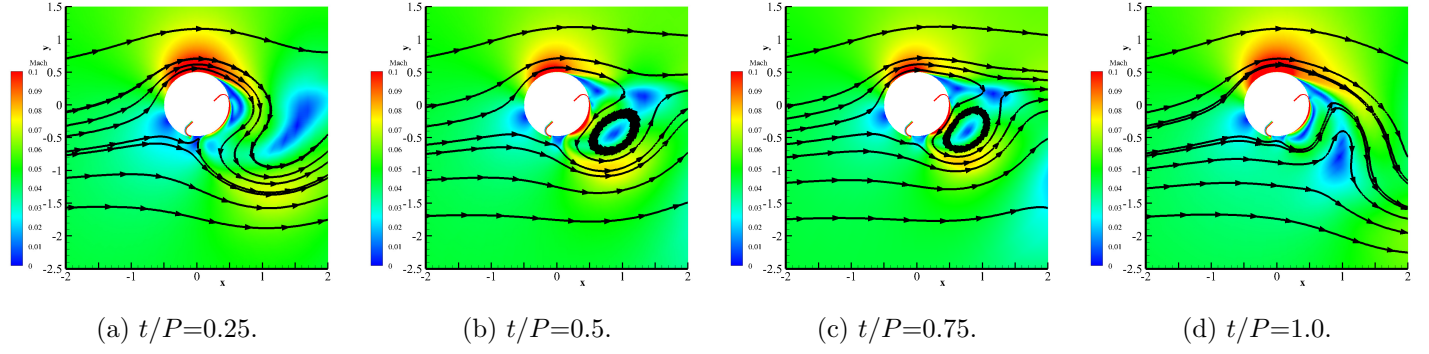
The second flow oscillation mode occurs at high lift coefficient with the flow mostly attached. The unsteadiness of flowfield is caused by the vortex shedding below the cylinder lower surface as shown in Fig. 16, which shows the variation of flowfield Mach contours around the cylinder with C_μ of 1.0, AoA=20° in an oscillation period. It shows the process of the vortex shedding and the oscillation of the detached stagnation point, which causes both the lift and drag oscillation.

(a) t/P=0.125. (b) t/P=0.25. (c) t/P=0.375. (d) t/P=0.5.

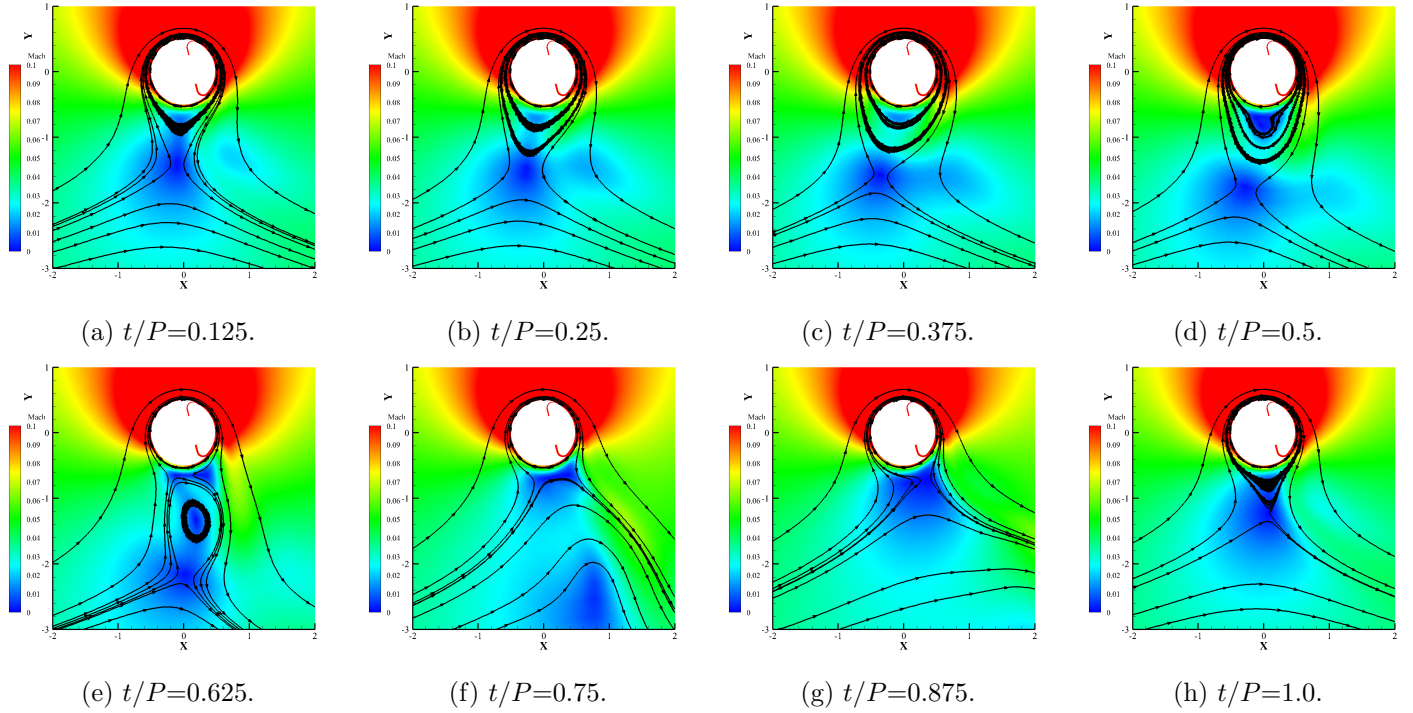(e) t/P=0.625. (f) t/P=0.75. (g) t/P=0.875. (h) t/P=1.0.

Figure 16: Mach Contours of Flowfields around the CFJ Cylinder with C_μ of 1.0, AoA=20° in a Period.

5 Conclusions

This paper numerically studies the performance of a 2D CoFlow Jet cylinder wind sail at different angle of attack and jet strength. The cylinder sail is simulated using the in-house Reynolds-averaged Navier-Stokes (RANS) solver,

FASIP, with Spalart-Allmaras (SA) turbulence model. A 3rd order WENO scheme is used to resolve the Navier-Stokes equations. The dual-time step method is used for unsteady simulation. A comparative analysis of the lift coefficients, drag coefficients and energy expenditure at various jet momentum coefficients and angles of attack are conducted. When $C_\mu = 0.5$, the lift coefficient at zero angle of attack reaches 12.63. The power coefficient at this flow condition is only 5% of C_L, resulting in a $C_L/C_{D,c}$ of 19.92. When C_μ is increased to 2.0, the lift coefficient reaches 25.13, about doubled, but the power coefficient is increased exponentially by 10 times. As AoA varies from -90° to 90°, the lift does not vary much within AoA of $\pm 20°$ at high C_L level of 20. At a lower C_L level of 12, the C_L has a much broader insensitive range to AoA from -20° to +60°. The drag coefficient and CFJ power coefficients are also similar. The numerical results of 2D CFJ cylinders indicate that the CFJ cylinder has the potential to provide very high lift coefficient at low drag and low power consumption with a large tolerance range of AoA. Such features are very beneficial as rigid wind sails for shipping.

6 Acknowledgment

References

[1] UNCTAD/RMT, *Review of Maritime Transport 2021*. United Nations, 2021.

[2] T. Sweeney, "Exploratory sailwing research at princeton," tech. rep., PRINCETON UNIV NJ, 1961.

[3] C. A. Marchaj, "Aero-hydrodynamics of sailing," *Adlard Coles Nautical an Imprint of A & C Black LTD Publishers, ISBN: 0-7136 3740 4, 2nd edition*, 1996.

[4] M. Gimbutas, *The goddesses and gods of Old Europe, 6500-3500 BC, myths and cult images*. Univ of California Press, 1982.

[5] D. Milić Kralj and B. Klarin, "Wing sails for hybrid propulsion of a ship," *Journal of Sustainable Development of Energy, Water and Environment Systems*, vol. 4, no. 1, pp. 1–13, 2016.

[6] G.-C. Zha and D. C. Paxton, "A Novel Flow Control Method for Airfoil Performance Enhancement Using Co-Flow Jet." *Applications of Circulation Control Technologies*, Chapter 10, p. 293-314, Vol. 214, Progress in Astronautics and Aeronautics, AIAA Book Series, Editors: Joslin, R. D. and Jones, G.S., 2006.

[7] G.-C. Zha, W. Gao, and C. Paxton, "Jet Effects on Co-Flow Jet Airfoil Performance," *AIAA Journal, No. 6,*, vol. 45, pp. 1222–1231, 2007.

[8] G.-C. Zha, C. Paxton, A. Conley, A. Wells, and B. Carroll, "Effect of Injection Slot Size on High Performance Co-Flow Jet Airfoil," *AIAA Journal of Aircraft*, vol. 43, 2006.

[9] G.-C. Zha, B. Carroll, C. Paxton, A. Conley, and A. Wells, "High Performance Airfoil with Co-Flow Jet Flow Control," *AIAA Journal*, vol. 45, 2007.

[10] Wang, B.-Y. and Haddoukessouni, B. and Levy, J. and Zha, G.-C., "Numerical Investigations of Injection Slot Size Effect on the Performance of Co-Flow Jet Airfoil," *Journal of Aircraft*, vol. Vol. 45, No. 6,, pp. pp.2084–2091, 2008.

[11] B. P. E. Dano, D. Kirk, and G.-C. Zha, "Experimental Investigation of Jet Mixing Mechanism of Co- Flow Jet Airfoil." AIAA-2010-4421, 5th AIAA Flow Control Conference, Chicago, IL, 28 Jun - 1 Jul 2010.

[12] B. P. E. Dano, G.-C. Zha, and M. Castillo, "Experimental Study of Co-Flow Jet Airfoil Performance Enhancement Using Micro Discreet Jets." AIAA Paper 2011-0941, 49th AIAA Aerospace Sciences Meeting, Orlando, FL, 4-7 January 2011.

[13] A. Lefebvre, B. Dano, W. Bartow, M. Difronzo, and G. Zha, "Performance and energy expenditure of coflow jet airfoil with variation of mach number," *Journal of Aircraft*, vol. 53, no. 6, pp. 1757–1767, 2016.

[14] A. Lefebvre, G-C. Zha, "Numerical Simulation of Pitching Airfoil Performance Enhancement Using Co-Flow Jet Flow Control," *AIAA paper 2013-2517*, June 2013.

[15] A. Lefebvre, G-C. Zha, "Cow-Flow Jet Airfoil Trade Study Part I : Energy Consumption and Aerodynamic Performance," *32nd AIAA Applied Aerodynamics Conference, AIAA AVIATION Forum, AIAA 2014-2682*, June 2014.

[16] A. Lefebvre, G-C. Zha, "Cow-Flow Jet Airfoil Trade Study Part II : Moment and Drag," *32nd AIAA Applied Aerodynamics Conference, AIAA AVIATION Forum, AIAA 2014-2683*, June 2014.

[17] Lefebvre, A. and Zha, G.-C., "Trade Study of 3D Co-Flow Jet Wing for Cruise Performance." AIAA Paper 2016-0570, AIAA SCITECH2016, AIAA Aerospace Science Meeting, San Diego, CA, 4-8 January 2016.

[18] Yang, Y.-C. and Zha, G.-C., "Super Lift Coefficient of Cylinder Using Co-Flow Jet Active Flow Control." AIAA Paper 2018-0329, AIAA SciTech Forum, 2018 AIAA Aerospace Sciences Meeting, Kissimmee, FL, 8-12 January 2018.

[19] McBreen, B. and Xu, K.-W. and Zha, G.-C., "Numerical Study of Extreme Adverse Pressure gradients Enabled by Co-Flow Jet." AIAA Paper 2023-1430, AIAA 2023 SciTech Forum, National Harbor, MD , 23-27 Jan. 2023.

[20] Zha, G.C., Shen, Y.Q. and Wang, B.Y., "An improved low diffusion E-CUSP upwind scheme ," *Journal of Computer and Fluids*, vol. 48, pp. 214–220, Sep. 2011.

[21] G.-C. Zha and E. Bilgen, "Numerical Study of Three-Dimensional Transonic Flows Using Unfactored Upwind-Relaxation Sweeping Algorithm," *Journal of Computational Physics*, vol. 125, pp. 425–433, 1996.

[22] B.-Y. Wang and G.-C. Zha, "A General Sub-Domain Boundary Mapping Procedure For Structured Grid CFD Parallel Computation," *AIAA Journal of Aerospace Computing, Information, and Communication*, vol. 5, No.11, pp. 2084–2091, 2008.

[23] Y.-Q. Shen, G.-C. Zha, and B.-Y. Wang, "Improvement of Stability and Accuracy of Implicit WENO Scheme ," *AIAA Journal*, vol. 47, pp. 331–344, 2009.